

Article

Impact of Ag Coating Thickness on the Electrochemical Behavior of Super Duplex Stainless Steel SAF2507 for Enhanced Li-Ion Battery Cases

Hyeongho Jo ^{1,†}, Jung-Woo Ok ^{2,†}, Yoon-Seok Lee ³, Sanghun Lee ¹, Yonghun Je ¹, Shinho Kim ¹ , Seongjun Kim ², Jinyong Park ², Jonggi Hong ², Taekyu Lee ² , Byung-Hyun Shin ^{2,*} , Jang-Hee Yoon ^{2,*}  and Yangdo Kim ^{1,*} 

¹ School of Materials Science and Engineering, Pusan National University, Busan 46241, Republic of Korea; cckk1224@naver.com (H.J.); comet0625@pusan.ac.kr (S.L.); wpydgns@naver.com (Y.J.); shinho@pusan.ac.kr (S.K.)

² Busan Center, Korea Basic Science Institute, Busan 46742, Republic of Korea; jwok@kbsi.re.kr (J.-W.O.); seongjunk@kbsi.re.kr (S.K.); jinyongp@kbsi.re.kr (J.P.); jkhong@kbsi.re.kr (J.H.); taekyulee1@kbsi.re.kr (T.L.)

³ AI-Realistic Media Research Department, Guri Electronic and Information Technology Research Institute, Gumi-si 39253, Republic of Korea; yslee@geri.re.kr

* Correspondence: lemonhouse211@kbsi.re.kr (B.-H.S.); jhyoon@kbsi.re.kr (J.-H.Y.); yangdo@pusan.ac.kr (Y.K.); Tel.: +82-10-974-6140 (B.-H.S. & J.-H.Y.); +82-10-3338-6208 (Y.K.)

† These authors contributed equally to this work.

Abstract: Li-ion batteries are at risk of explosions caused by fires, primarily because of the high energy density of Li ions, which raises the temperature. Battery cases are typically made of plastic, aluminum, or SAF30400. Although plastic and aluminum aid weight reduction, their strength and melting points are low. SAF30400 offers excellent strength and corrosion resistance but suffers from work hardening and low high-temperature strength at 700 °C. Additionally, Ni used for plating has a low current density of 25% international copper alloy standard (ICAS). SAF2507 is suitable for use as a Li-ion battery case material because of its excellent strength and corrosion resistance. However, the heterogeneous microstructure of SAF2507 after casting and processing decreases the corrosion resistance, so it requires solution heat treatment. To address these issues, in this study, SAF2507 (780 MPa, 30%) is solution heat-treated at 1100 °C after casting and coated with Ag (ICAS 108.4%) using physical vapor deposition (PVD). Ag is applied at five different thicknesses: 0.5, 1.0, 1.5, 2.0, and 2.5 μm. The surface conditions and electrochemical properties are then examined for each coating thickness. The results indicate that the PVD-coated surface forms a uniform Ag layer, with electrical conductivity increasing from 1.9% ICAS to 72.3% ICAS depending on the Ag coating thickness. This enhancement in conductivity can improve Li-ion battery safety on charge and use. This result is expected to aid the development of advanced Li-ion battery systems in the future.

Keywords: Ag coating; super duplex stainless steel; Li-ion battery case; physical vapor deposition; electrochemical behavior



Academic Editors: Wenbo Wang, Auezhan Amanov and Zhengwu Fang

Received: 23 December 2024

Revised: 1 January 2025

Accepted: 7 January 2025

Published: 9 January 2025

Citation: Jo, H.; Ok, J.-W.; Lee, Y.-S.; Lee, S.; Je, Y.; Kim, S.; Kim, S.; Park, J.; Hong, J.; Lee, T.; et al. Impact of Ag Coating Thickness on the Electrochemical Behavior of Super Duplex Stainless Steel SAF2507 for Enhanced Li-Ion Battery Cases. *Crystals* **2025**, *15*, 62. <https://doi.org/10.3390/cryst15010062>

Crystals **2025**, *15*, 62. <https://doi.org/10.3390/cryst15010062>

Copyright: © 2025 by the authors. Licensee MDPI, Basel, Switzerland. This article is an open access article distributed under the terms and conditions of the Creative Commons Attribution (CC BY) license (<https://creativecommons.org/licenses/by/4.0/>).

1. Introduction

Li-ion batteries exhibit outstanding performance and are considered excellent candidates as power sources for various applications, including electric vehicles (EVs) and portable electronic devices [1,2]. Since 2010, the demand for portable electronic devices such as smartphones and tablets has increased substantially, and from 2020, the demand for EVs has surged significantly [3,4]. However, safety concerns related to the high-temperature

ignition of these batteries (rising up to 700 °C) have been continuously reported and require urgent attention [5,6]. Researchers have been investigating battery systems through system-level studies to control battery ignition and thereby improve safety [7,8]. For instance, Tudoroiu studied temperature management systems for batteries, while Rahman focused on developing warning systems associated with battery temperature [9]. Despite these efforts, the heat generated by direct Li electron emissions remains uncontrolled, and research on improving the materials used in batteries remains limited.

The ignition of batteries is primarily triggered by the thermal runaway of the battery [10,11]. Therefore, enhancing electrical conductivity when Li is directly involved can reduce heat generation [12]. Current systems have attempted to improve electrical conductivity by coating the battery case with Ni [13]. Although Ni has a relatively low electrical conductivity of 23.8% international copper alloy standard (ICAS), it still exceeds that of the case material, thereby reducing heat generation caused by electrical resistance. Several materials, such as Ag (108.4% ICAS) and Cu (100.0% ICAS), exhibit higher electrical conductivity than Ni. However, despite Ag's high electrical conductivity, its high cost has prevented its widespread use as a coating. The existing literature typically focuses on Ni plating on SAF30400, with limited studies exploring other coatings.

Initially, battery cases were made from plastic, with aluminum alloys later introduced to improve safety [4,14,15]. Although aluminum alloys possess excellent strength and corrosion resistance, their low melting point (670 °C) makes them unsuitable for withstanding high-temperature ignition (700 °C). The more recently adopted material, SAF30400 (austenite stainless steel), offers both strength and corrosion resistance. However, it faces challenges such as low high-temperature strength (170 MPa at 700 °C), a high thermal expansion coefficient (19.5×10^{-6} at 700 °C), and susceptibility to work hardening under stress [16,17]. These issues not only shorten the lifespan of the battery case material but complicate the recycling process. Therefore, selecting recyclable materials with excellent strength and corrosion resistance is essential.

Super-duplex stainless steel (SDSS) is a dual-phase stainless steel consisting of austenite and ferrite, which provides excellent strength and corrosion resistance. Additionally, it has high high-temperature strength (340 MPa at 700 °C) and low thermal expansion coefficient (14.0×10^{-6}), making it suitable for use in battery cases. Its high strength (780 MPa) and corrosion resistance (with a durability of up to 50 years in seawater) suggest that it can be efficiently recycled when used in Li-ion battery cases [18,19]. Therefore, the adoption of SDSS in battery cases is expected to significantly improve safety.

Research on SDSS has been extensive, particularly during its early development stages for manufacturing [20,21]. Various researchers have studied SDSS, with Nillson analyzing the heat treatment conditions for optimizing its properties [19,22]. Recent studies have shifted focus toward the application of SDSS in various fields, with Nando, for instance, researching the laser welding of SDSS. Despite extensive research on SDSS, studies on its practical applications remain limited. Moreover, no research has specifically investigated the use of SDSS as a material for Li-ion battery cases.

This study utilized SDSS SAF2507, renowned for its excellent strength and corrosion resistance, and applied Ag coating to enhance the electrical conductivity of lithium-ion batteries. The thickness of the Ag coating was precisely controlled, and its properties were thoroughly analyzed. Surface images corresponding to various coating thicknesses were examined, and their electrochemical characteristics were evaluated through specialized methods.

2. Experimental Methods

2.1. Manufacture of Super Duplex Stainless Steel SAF2507

In this study, the material was cast in an electric furnace and subsequently solution heat-treated. The specimen preparation process and experimental conditions are presented in Figure 1. The specimens (# α) used in the experiments were cast in an electric furnace and air-cooled (POSCO SS, Changwon, Republic of Korea) [19,23]. Due to issues such as uneven microstructure and alloy segregation observed in the cast specimens, solution heat treatment was performed at 1100 °C for 1 h (# β) to address these problems [24,25]. The microstructures of both the cast and solution heat-treated specimens were analyzed using FE-SEM (SUPRA 40VP system, Zeiss, Oberkochen, Germany). In addition, the composition of each phase was analyzed using energy-dispersive X-ray spectroscopy (EDS; SUPRA 40VP system, Zeiss, Oberkochen, Germany) [26,27]. The phase fractions were determined from the FE-SEM images, and tests were repeated five times to verify consistency based on different specimen locations.

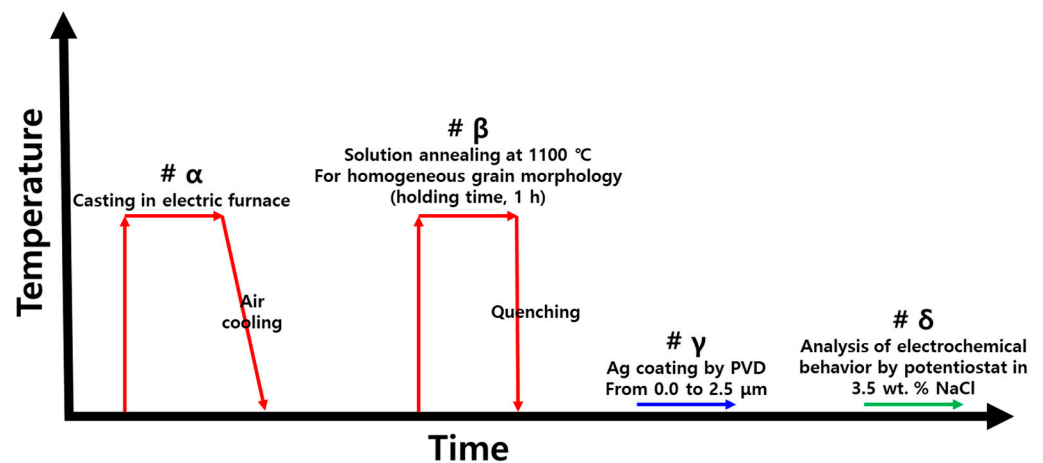


Figure 1. Schematic diagram of the preparation and analysis timeline of Ag-coated super duplex stainless steel SAF2507: (# α) casting for manufacturing (red arrow), (# β) solution annealing to achieve homogeneous grains (red arrow), (# γ) Ag coating applied via PVD in thicknesses ranging from 0.0 to 2.5 μm (blue arrow), and (# δ) analysis of electrochemical behavior (green arrow).

The primary alloys in the cast material were Cr, Ni, and Mo, with their chemical compositions analyzed using inductively coupled plasma mass spectrometry (ICP-MS; Thermo Fisher Scientific, Waltham, MA, USA); the results are presented in Table 1. The chemical analysis revealed that the primary alloys contained 25.2 wt.% Cr, 3.8 wt.% Mo, and 6.8 wt.% Ni [28,29]. Duplex stainless steels are classified based on the calculated pitting resistance equivalent number (PREN), which contributes to strengthening the passive layer, as presented in Equation 1.

$$\text{PREN} = \text{wt.}\% \text{ Cr} + 3.3 \text{ wt.}\% \text{ Mo} + 16 \text{ wt.}\% \text{ N}, \quad (1)$$

Table 1. Chemical composition of Ag-coated super duplex stainless steel SAF2507, as determined by ICP-MS (unit: wt.%) [19,30].

	C	N	Mn	Ni	Cr	Mo	Fe	PREN
Chemical composition	0.01	0.27	0.8	6.8	25.2	3.8	Bal	41.8

The PREN of the cast material was 41.8, classifying it as SDSS (40–50) [17,31]. The chemical composition of the material was comparable to that of SDSS SAF2507. Among

the primary alloys, Cr predominantly forms the passivation layer (Cr_2O_3) in stainless steel [32,33]. Mo exhibits a larger lattice structure than Cr, thus acting as an accelerator for Cr passivation [34]. N, an interstitial element, remains within the lattice and further enhances Cr passivation [16,35,36]. Ni and Mn are austenite-stabilizing elements that contribute to the stabilization of the austenite phase [17].

2.2. Conditions for Producing the Ag Coating and Methods of Its Analysis

To use SDSS SAF2507 as a battery case, enhancing its electrical conductivity is essential. While existing studies have improved electrical conductivity using Ni, we applied an Ag coating to achieve superior performance for the battery case. The Ag coating was applied using PVD (Laon Tech, Anseong-si, Republic of Korea) [13,37]. The conditions for Ag coating via PVD are listed in Table 2. Ag was evaporated using a current of 80 A, with coating durations ranging from 10 to 40 min.

Table 2. PVD conditions (current, vapor time, pressure) for Ag coating of super duplex stainless SAF2507 to enhance Li-ion battery case performance.

	Current, A	Vapor Time, Min	Pressure, Torr
Value	80	10–40	1.2×10^{-6}

The surface conditions of the SDSS SAF2507 after Ag coating were analyzed using FE-SEM, XRD (D8 Venture, Stanford, CA, USA), atomic force microscopy (AFM), and GDS (Horiba Jobin Yvon, JY-10000 RF, Palaiseau, France). FE-SEM was used to examine surface images based on Ag coating thickness [37,38]. XRD was used to analyze phase changes on the surface under various Ag coating conditions, scanning an area of 1 cm^2 from 20° to 80° with a step size of $0.5^\circ/\text{s}$ [39,40]. The surface roughness concerning Ag coating thickness was evaluated using AFM (Park System, Suwon, Korea), with a measurement length of $50 \text{ }\mu\text{m}$. Roughness was based on average maximum and average values, determined by averaging measurements from five different locations. The thickness of the coating layer was measured using GDS. For a comprehensive analysis of the Ag coating layer, the concentrations of Ag, Ni, Fe, Mo, and Cr were determined using GDS, with an analysis area of 4 cm^2 and a depth of $5 \text{ }\mu\text{m}$.

2.3. Analysis of Electrochemical Behavior

The electrochemical behavior concerning Ag coating thickness was investigated using three methods: OCP, EIS, and potentiodynamic polarization tests. Analysis was conducted using a potentiostat (VersaSTAT 4.0, AMETEK, Inc., Berwyn, PA, USA) within a three-electrode cell configuration. The cell consisted of a working electrode (WE, specimen) with an analysis surface area of 1 cm^2 , a counter electrode (CE, Pt mesh, $20 \times 20 \text{ mm}$), and a reference electrode (RE, saturated calomel electrode (SCE)). A 3.5 wt.% NaCl solution, as specified in ASTM G 61, served as the electrolyte [41].

The potential of a material is influenced by the properties of the metal, making it challenging to calculate based solely on alloying metal or surface conditions. Therefore, the OCP was measured, reflecting the potential of hydrogen and oxygen reactions over time in the electrolyte solution [42,43]. OCP measurements were conducted for 3600 s at a step rate of 1 point/s. Potentiodynamic polarization tests assessed corrosion behavior by measuring changes in current density relative to the applied voltage. These tests were conducted by applying voltages ranging from -0.6 to 1.2 V at a scan rate of 0.167 mV/s , allowing for an evaluation of electrochemical reactions based on Ag coating thickness [31].

3. Results

3.1. Manufacture of SDSS SAF2507

SDSS SAF 2507 is characterized by its high alloy content, necessitating precise control of chemical composition during the electric furnace process. Following casting, SAF 2507 undergoes solution annealing. After manufacturing, the material may be subjected to machining, welding, and coating before being utilized in applications such as battery casings. The microstructures of SAF 2507 after casting and solution heat treatment are presented in Figure 2.

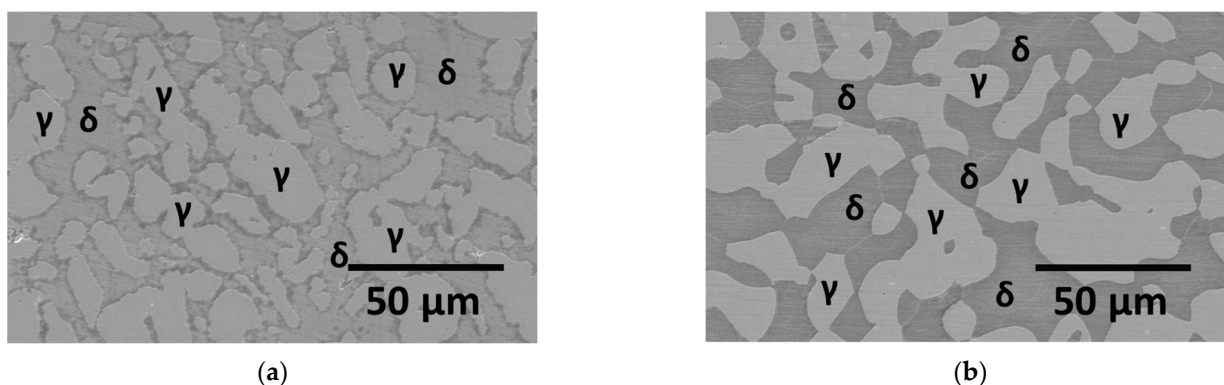


Figure 2. FE-SEM images illustrating the manufacturing process of super duplex stainless steel SAF2507: (a) casting and (b) solution annealing at 1100 °C.

The as-cast microstructure exhibits an inhomogeneous distribution of austenite (γ , bright gray islands) and ferrite (δ , base matrix). Post-casting, austenite is differentiated into coarse and fine grains, with coarse austenite grains exceeding 20 μm in diameter and fine grains measuring less than 3 μm [19,44]. This inhomogeneous morphology of austenite arises from variations in nucleation and growth energies, influenced by the chemical compositional differences within the SAF 2507 alloy. Ferrite appears in areas with both high and low volume fractions; regions with a high ferrite volume fraction result from insufficient driving force for austenite nucleation. Conversely, fine austenite grains are evident in areas with a lower ferrite fraction. The air-cooled as-cast microstructure exhibits alloy segregation, leading to differences in nucleation and growth energies, which ultimately affect the microstructural morphology.

Solution Annealing stabilizes the microstructure of SAF 2507. The heat-treated microstructure shows a reduced volume fraction of fine austenite grains and a decrease in the variability of ferrite volume fractions. Uniform grain growth occurs, with austenite grain diameters increasing from 5 to 25 μm , which mitigates ferrite segregation. This process promotes the formation of homogeneously sized austenite grains, contributing to the overall stabilization of both ferrite and austenite phases.

The microstructure of SAF 2507 experiences significant changes in volume fractions following solution annealing, as shown in Figure 3. Prior to solution heat treatment, the volume fraction of austenite measured 56.1%, surpassing that of ferrite. However, post-solution annealing, the volume fractions of austenite and ferrite became equal, with the variation in volume fraction decreasing from 4.2% to 2.6%. This indicates that solution annealing plays a critical role in stabilizing the volume fractions of austenite and ferrite.

The equalization of volume fractions post-heat treatment contributes to enhanced corrosion resistance by balancing the electrochemical potentials between austenite and ferrite, thereby reducing galvanic corrosion. Nilsson's study on the corrosion resistance of SAF 2507 under various solution-annealing conditions supports this finding, demonstrating

optimized corrosion resistance achieved through balanced volume fractions of austenite and ferrite.

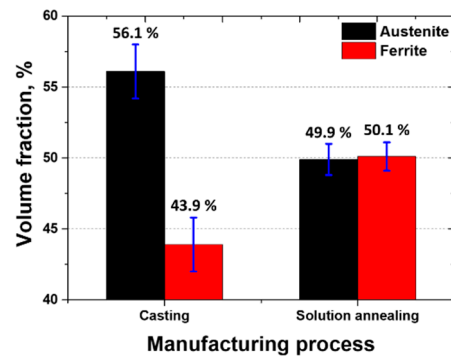


Figure 3. Volume fractions of austenite and ferrite in super duplex stainless steel SAF2507 for various manufacturing processes.

Consequently, the final microstructural state of SAF 2507 during the manufacturing process is stabilized through solution heat treatment. This treatment results in a homogenized microstructure, which is essential for achieving optimized corrosion resistance.

3.2. Effect of Ag Coating

To enhance the manufacturing of Li-ion battery cases, SDSS SAF2507 was coated with Ag instead of Ni, with the surface analyzed using FE-SEM, as shown in Figure 4. The surface images reveal variations that depend on the coating thickness. A smooth, mirror-like finish was achieved through surface pretreatment prior to coating. The surface characteristics exhibited coating distinct features based on the Ag coating thickness. At a thickness of 0.5 μm , the surface appeared fine and heterogeneous, displaying microstains. As the thickness increased to 2.0 μm , the surface became significantly more uniform.

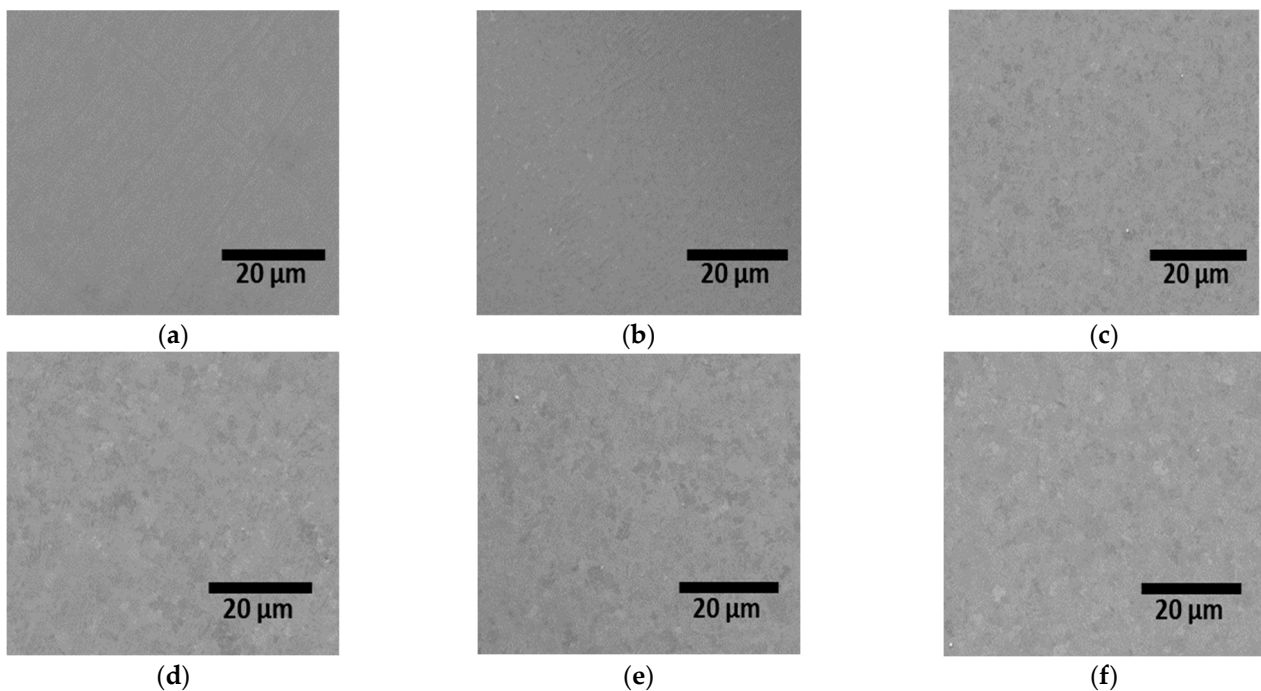
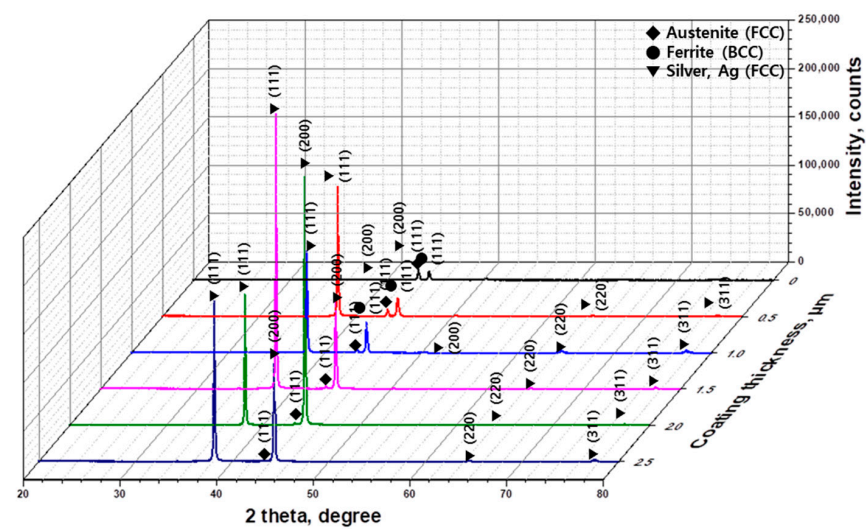
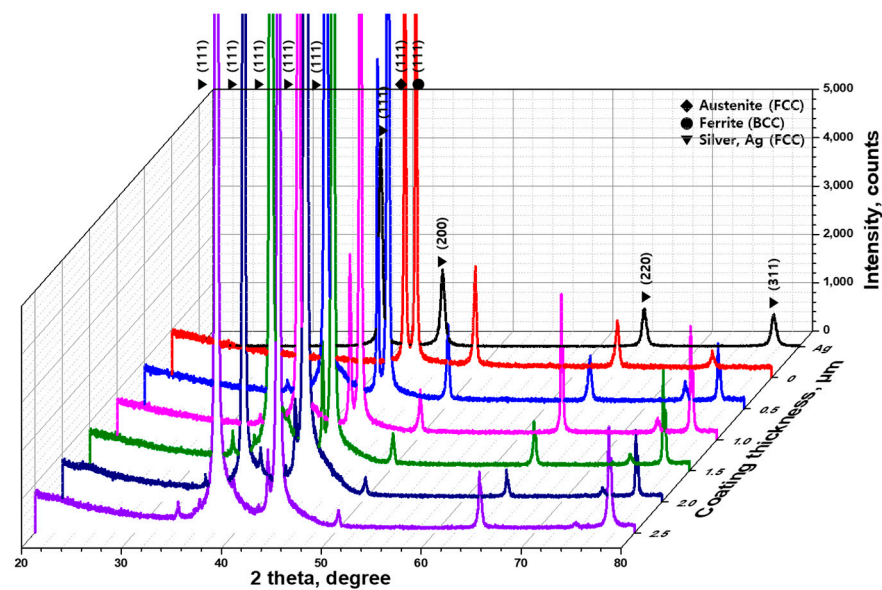


Figure 4. Surface images of Ag-coated super duplex stainless steel SAF2507 with varying Ag coating thicknesses for enhanced Li-ion battery case applications: (a) coating thickness = 0.0 μm (before coating), (b) coating thickness = 0.5 μm , (c) coating thickness = 1.0 μm , (d) coating thickness = 1.5 μm , (e) coating thickness = 2.0 μm , and (f) coating thickness = 2.5 μm .

The influence of Ag coating on the microstructure was analyzed using X-ray diffraction (XRD), with results depicted in Figure 5. The primary growth of austenite and ferrite in SDSS was observed on the (111) plane at approximately 42° and 45° . This growth further extended to the (200) planes at 51° and 65° and to the (220) plane at 73° . The main peaks of SAF2507 were consistent with those reported in the existing literature, indicating typical states. Notably, the intensity of the SAF2507 peaks exhibited a decreasing trend with increasing Ag coating thickness, while the intensity of the Ag peaks demonstrated an increasing trend. The behavior of the Ag peaks varied with the coating thickness; specifically, the Ag (111) plane served as the primary growth peak up to a thickness of $1.5\ \mu\text{m}$, after which the growth shifted toward the (200) direction beyond $2.0\ \mu\text{m}$. These results indicate the influence of the matrix structure on the growth behavior. The primary growth direction for SAF2507 was along the (111) plane, and Ag coated up to $1.5\ \mu\text{m}$ also aligned with this plane. Beyond this thickness, the surface images exhibited more complexity, suggesting changes in microstructural characteristics.



(a)



(b)

Figure 5. XRD patterns for SDSS SAF2507 with varying Ag coating thicknesses for enhanced Li-ion battery cases: (a) intensity from 0 to 250,000 and (b) intensity from 0 to 5000.

The surface of SDSS SAF2507 was polished and electropolished to facilitate Ag coating, maintaining a surface roughness of less than 10 nm. The surface roughness was analyzed using AFM, with the results presented in Figure 6. The roughness exhibited a decreasing trend with increasing Ag coating thickness, reaching 2 nm at a thickness of 1.5 μm . This reduction in roughness up to 1.5 μm is attributed to preferential coating on the (111) plane, where the influence of the base microstructure was significant. Beyond 1.5 μm , an increase in surface roughness was observed due to the growth of the (200) and (220) planes. Consequently, the lattice structures of both the base microstructure and metal lattice structure significantly influenced the surface roughness. In metals, an increase in surface roughness acts as a factor that reduces electrical conductivity because it increases the move distance of electrons and dislocation [37,45]. At 2.5 μm , an increase in surface roughness can hinder the improvement of electrical conductivity.

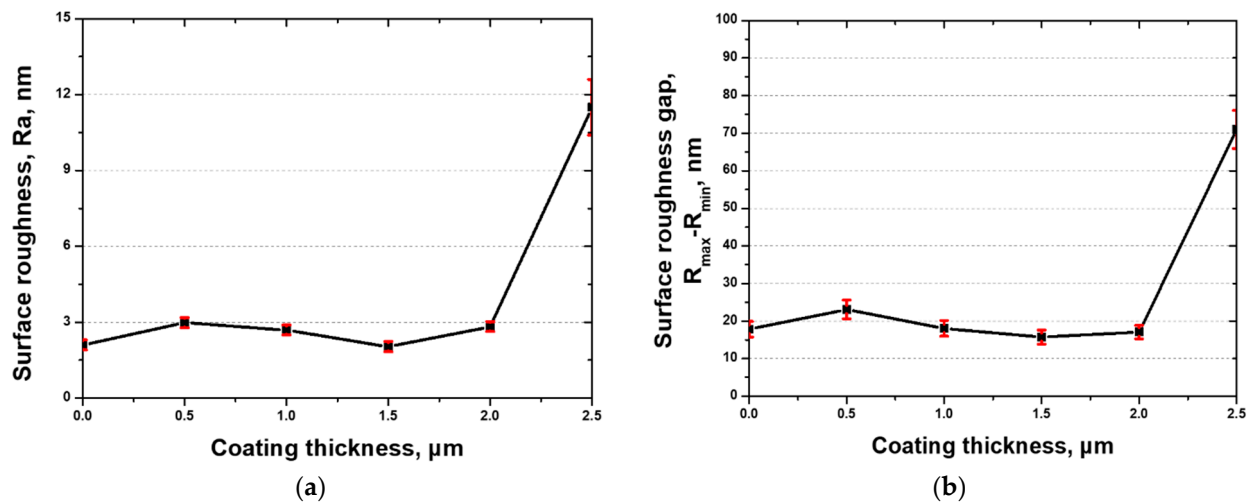


Figure 6. Surface roughness of Ag-coated super duplex stainless steel SAF2507 at varying coating thicknesses from 0 to 2.5 μm : (a) Ra (μm) and (b) roughness gap, defined as the difference between the maximum and minimum roughness (μm).

The coating thickness was analyzed using GDS, with the results presented in Figure 7. The Ag coating layer was classified into two distinct states: the coating layer and the mixed layer. The coating layer exhibited a high Ag density of over 99%, whereas the mixed layer showed a decreased Ag concentration alongside an increase in the concentrations of SAF2507 elements. The components of SAF2507, such as Ni, Fe, Mo, and Cr, exhibited similar behaviors before and after coating. These observed differences were attributed to the extended results dependent on the Ag coating layer. Therefore, the conditions of SAF2507 remained consistent, with variations noted only in the Ag coating layer, as confirmed by GDS. The GDS analysis revealed the thickness of the Ag coating layer and validated the presence of a mixed layer, confirming that the coating thickness matched the designed specifications.

The Ag-coated SDSS exhibited enhanced electrical conductivity at Figure 8, which was assessed by measuring electrical resistance [37,45]. In this context, the ICAS defined the conductivity of Cu at 100%, Fe at 1.9%, and Ag at 108.4%. The electrical conductivity demonstrated a dependence on the thickness of the Ag coating. At an Ag coating thickness of 0.0 μm , the ICAS was recorded at 1.9%, increasing to 58.8% at 1.0 μm . However, this upward trend diminished as the thickness increased, reaching 72.3% at 2.5 μm . Although the Ag coating layer contributed to enhancing electrical conductivity, this improvement appeared to be influenced by both the coating thickness and the underlying lattice structure.

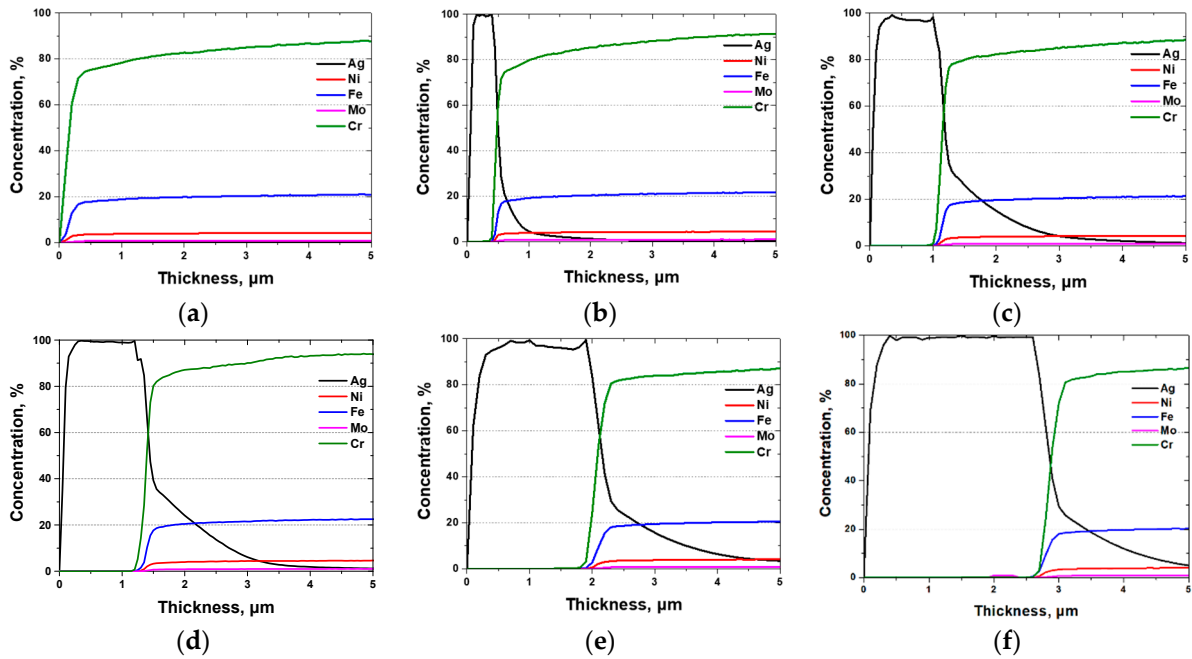


Figure 7. GDS results illustrating the relationship between thickness (μm) and the concentration of major alloying elements (%) in SDSS SAF2507 with various Ag coating thicknesses, employed in enhanced Li-ion battery cases: (a) coating thickness = 0.0 μm (before coating), (b) coating thickness = 0.5 μm , (c) coating thickness = 1.0 μm , (d) coating thickness = 1.5 μm , (e) coating thickness = 2.0 μm , and (f) coating thickness = 2.5 μm .

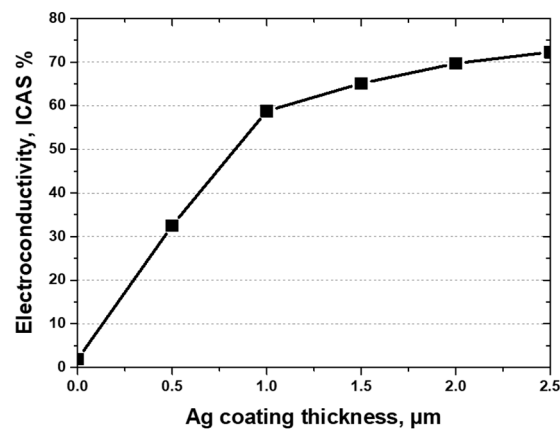


Figure 8. Electrical conductivity as a function of Ag coating thickness on SDSS SAF2507.

Although electrical conductivity increased with the thickness of the Ag coating, the rate of increase was dependent on the lattice orientation. A uniform Ag coating layer on the (111) plane exhibited an ICAS electrical conductivity exceeding 57% at 1 μm . In contrast, Ag coating layers grown in various orientations showed an ICAS conductivity of only 23.5%, indicating that lattice structure significantly affected electron movement. Previous studies have shown that electrical steel oriented along the (111) plane, achieved through rapid cooling rates, exhibits excellent electrical properties. The conductivity characteristics observed in this study align with earlier findings, highlighting that controlling the lattice structure of the coating layer is a critical factor for optimizing electrical conductivity.

3.3. Electrochemical Behavior

The reactivity of pure metals can be calculated using the electrons involved in the reaction and the Nernst equation to determine the galvanic potential. However, it is

difficult to calculate the reactivity of alloys or surface-treated materials because the surface treatment affects the reactivity [46,47]. Therefore, the potential of the surface-treated alloys can be measured using the OCP. The OCP results for different Ag coating thicknesses are presented in Figure 9. As the Ag coating thickness increases, the potential decreases from -0.04 to -0.11 V. The potential continuously decreases with increasing Ag coating thickness, with the largest drop observed at a thickness of $0.5 \mu\text{m}$, where the potential reaches -0.08 V.

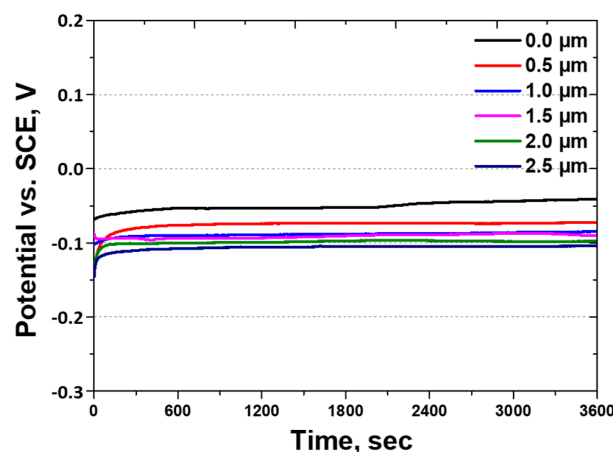


Figure 9. Time (s) vs potential (V) curve, i.e., OCP curve for various Ag coating thicknesses on super duplex stainless steel SAF2507 in NaCl electrolyte solution of 3.5 wt.%.

The potential of stainless steel varies depending on the surface condition and is generally known to range between -0.3 and 0.1 V [48,49]. The potential of SDSS SAF2507 before the coating was -0.04 V, which aligns with the existing theoretical values. The Ag layer coated on the surface of SDSS influences its potential. Because Ag, with an atomic number of 47, is larger than Cl, which has an atomic number of 17, the Ag coating layer provides sufficient space for Cl ions to penetrate. Consequently, the decrease in potential observed in the OCP results is due to the galvanic corrosion between Ag and SDSS, leading to a reduction in the potential. As the coating thickness increases, the galvanic potential increases, which explains the decrease in the potential observed in the OCP results.

The potentiodynamic polarization test can predict the corrosion behavior by observing changes in the current density in relation to the potential [31,41]. To analyze the corrosion behavior based on the thickness of the coating layer, a potentiodynamic polarization test was conducted, and the results are presented in Figure 10 and Table 3. Before coating, SDSS SAF2507 exhibited activation polarization at -0.1 V, and after passivation, the pitting potential (E_{pit}) was confirmed at 1.11 V. After coating, the potential during activation polarization decreased and the current density increased. In addition, the pitting potential decreased.

Table 3. Key values of OCP results and parameters from potentiodynamic polarization curves for various Ag coating thicknesses up to $2.5 \mu\text{m}$ on SDSS SAF2507.

Ag Coating Thickness, nm	OCP Potential, V	Potentiodynamic Polarization Curve at Active Polarization		
		E_{corr} , V	I_{corr} , A/cm ²	E_{pit} , V
0.0	-0.04	-0.09	2×10^{-7}	1.11
0.5	-0.07	-0.10	4×10^{-7}	1.00
1.0	-0.09	-0.11	4×10^{-7}	1.03
1.5	-0.09	-0.11	4×10^{-7}	1.04
2.0	-0.11	-0.12	4×10^{-7}	1.03
2.5	-0.11	-0.21	4×10^{-5}	0.03

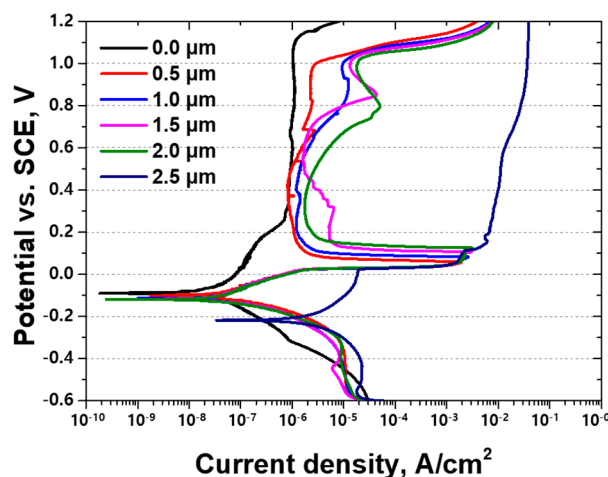


Figure 10. Potentiodynamic polarization curves displaying the relationship between potential (V) and current density (A/cm^2) for SDSS SAF2507 with varying Ag coating thicknesses.

The Ag coating on the SDSS surface accelerated the corrosion rate owing to galvanic corrosion. During the passivation stage, uneven corrosion occurred on the Ag-coated material. The Ag coating influenced the corrosion behavior, resulting in reduced corrosion resistance. As the thickness of the Ag coating increased, the corrosion rate from galvanic corrosion also rose, leading to accelerated corrosion during activation polarization and a decrease in the pitting potential [50,51]. This behavior varied with coating thickness. While galvanic corrosion increased from $0.5 \mu\text{m}$ to $2.0 \mu\text{m}$, the rate of increase at thicknesses above $2.5 \mu\text{m}$ escalated significantly, resulting in uniform corrosion at 0.03 V . The Ag coating appeared to shift the corrosion of SDSS SAF2507 toward uniform corrosion [52,53]. Based on the results of the potentiodynamic polarization test, maintaining the Ag coating layer inside battery cases below $2.0 \mu\text{m}$ is advisable.

To measure corrosion caused by Cl^- ions, the atomic radius was calculated using the covalent radius. Results are presented in Table 4 and Figure 11. Stainless steel exhibits passive ceramic polarization, with a mass of $152.0 \text{ g}/\text{m}^3$ and an atomic radius of up to 440 pm . XRD analysis showed that the primary growth direction of SDSS SAF2507 aligned with the (111) plane, which also served as the initial plating growth plane for Ag. However, starting from the second layer, gaps altered the growth direction of the coating, leading to the formation of voids as coating thickness increased. This change in growth direction reduced the available spaces for Cl^- ion penetration, which subsequently increased galvanic corrosion.

Table 4. Values of atomic number, atomic mass, and atomic radius for each element present in the passivation layer.

Element	Atomic Number	Mass, g/m^3	Atom Radius, pm
Cr	24	52.0	130
Ag	47	107.9	160
O	8	16.0	60
Cl	17	35.5	100

An increase in the thickness of the Ag coating led to more pronounced galvanic corrosion. This was attributed to the surface reaction between Ag and SDSS SAF2507, accompanied by a rise in the corrosion rate from 2×10^{-7} to 4×10^{-5} . This corrosion behavior was strongly influenced by surface conditions. Figure 11 illustrates an uneven Ag coating (highlighted by the red dashed square) on the surface of SDSS SAF2507, where

the growth of the coating layer occurred predominantly in the (111) direction. The lattice mismatch introduced uneven gaps, diversifying the growth directions of the coating and partially filling these gaps. However, the coating failed to fully seal the gaps, which allowed uniform corrosion to proceed after activation polarization during the potentiodynamic polarization test. To mitigate this corrosion issue, the formation of a new intermediate layer—comprising materials with low atomic size and high density—between the stainless steel and the silver coating can be proposed. This intermediate layer could act as a buffer to reduce galvanic corrosion.

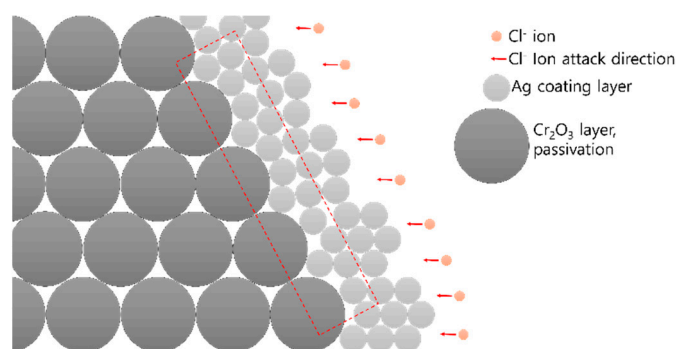


Figure 11. Image depicting chloride ion attack on Ag-coated SDSS SAF2507 in an electrolyte solution.

Previous research has indicated the difficulty of achieving a completely sealed coating layer using both wet and dry coating methods. The electrochemical analysis results from this study confirmed these trends. Coating SDSS with Ag up to a thickness of 2.5 μm resulted in inadequate corrosion resistance, highlighting the desirability of maintaining a coating thickness of 2.0 μm .

4. Conclusions

Ag coating to a thickness of 2.5 μm influenced the corrosion resistance of SDSS SAF2507, as indicated by the electrochemical analysis results from this study.

(1) After casting and heat treatment, the microstructure and phase fraction of SDSS SAF2507 were stabilized through solution annealing. The as-cast microstructure formed a ferrite matrix with uneven austenite grains ranging from 5 to 50 μm . Additionally, the volume fraction of austenite exceeded 56%. Following the solution heat treatment, the austenite grain size was homogenized to 20–30 μm , equivalent to that of ferrite. This solution annealing process has secured the machining conditions for the material, ensuring superior corrosion resistance and mechanical properties, making it suitable for component manufacturing. These conditions are suitable to be applied to the manufacturing process of SDSS because they control the organization during manufacturing.

(2) The Ag coating on SDSS SAF2507 was influenced by the base structure, with the primary growth direction along the (111) plane up to a coating thickness of 1.5 μm . The surface roughness decreased to below 2 nm up to a coating thickness of 2.0 μm but increased to 6 nm at 2.5 μm . The roughness of the Ag coating layer occurred at the nanometer scale and depended on the growth direction. Electrical conductivity varied with coating thickness, with differences influenced by both thickness and lattice structure. Therefore, managing the lattice structure of the coating layer is essential in addition to controlling the thickness. Therefore, it was confirmed that metal coating is possible on dual-phase materials.

(3) Differences in electrochemical behavior were observed depending on Ag coating thickness. Increasing the thickness of the Ag coating resulted in a decrease in potential due to galvanic corrosion, shifting from -0.04 V to -0.11 V, while the corrosion rate (current

density) increased from 2.6×10^{-7} A/cm² to 4.0×10^{-5} A/cm². The Ag coating decreased corrosion resistance due to galvanic corrosion as a result of the formation of a passivation layer on SDSS. However, when the coating thickness was below 2.0 μ m, SDSS SAF2507 maintained passivation, preserving excellent corrosion resistance. Therefore, implementing a pre-coating strategy when applying a coating to SDSS SAF2507 is crucial for maintaining high electrical conductivity without compromising corrosion resistance. Through this study, the possibility of improving Li-ion battery case materials was confirmed and it is expected to be helpful in the development of structural materials for electronic products in the future.

Author Contributions: Conceptualization, H.J., S.K. (Shinho Kim), B.-H.S., Y.K. and J.-H.Y.; methodology, S.K. (Shinho Kim), S.L., J.-W.O., Y.-S.L. and J.P.; software, S.L., J.-W.O., Y.-S.L. and J.P.; validation, Y.J., S.K. (Seongjun Kim), J.H. and T.L.; formal analysis, S.K. (Seongjun Kim), J.H. and T.L.; investigation, Y.J., H.J., and B.-H.S.; resources, Y.K., Y.-S.L. and J.H.; data curation, H.J. and B.-H.S.; writing—original draft preparation, H.J. and B.-H.S.; writing—review and editing, H.J. and B.-H.S.; supervision, H.J. and B.-H.S.; project administration, Y.K. and J.-H.Y.; funding acquisition, Y.K. and J.-H.Y. All authors have read and agreed to the published version of the manuscript.

Funding: This work was supported by a grant from the Korea Basic Science Institute (grant number A412220).

Data Availability Statement: The original contributions presented in this study are included in the article. Further inquiries can be directed to the corresponding authors.

Conflicts of Interest: The authors declare no conflicts of interest.

References

1. Park, J.; Fatima, S.A. A DFT Study of TiC₃ as Anode Material for Li-Ion Batteries. *Appl. Surf. Sci.* **2023**, *638*, 158024. [CrossRef]
2. Chang, W.-S.; Park, C.-M.; Kim, J.-H.; Kim, Y.-U.; Jeong, G.; Sohn, H.-J. Quartz (SiO₂): A New Energy Storage Anode Material for Li-Ion Batteries. *Energy Environ. Sci.* **2012**, *5*, 6895–6899. [CrossRef]
3. Bizeray, A.M.; Howey, D.A.; Monroe, C.W. Resolving a Discrepancy in Diffusion Potentials, with a Case Study for Li-Ion Batteries. *J. Electrochem. Soc.* **2016**, *163*, E223. [CrossRef]
4. Cicconi, P.; Kumar, P.; Varshney, P. A Support Approach for the Modular Design of Li-Ion Batteries: A Test Case with PCM. *J. Energy Storage* **2020**, *31*, 101684. [CrossRef]
5. Rahman, A.; Lin, X.; Wang, C. Li-Ion Battery Anode State of Charge Estimation and Degradation Monitoring Using Battery Casing via Unknown Input Observer. *Energies* **2022**, *15*, 5662. [CrossRef]
6. Klink, J.; Hebenbrock, A.; Grabow, J.; Orazov, N.; Nylén, U.; Bengler, R.; Beck, H.-P. Comparison of Model-Based and Sensor-Based Detection of Thermal Runaway in Li-Ion Battery Modules for Automotive Application. *Batteries* **2022**, *8*, 34. [CrossRef]
7. Petit, M.; Prada, E.; Sauvant-Moynot, V. Development of an Empirical Aging Model for Li-Ion Batteries and Application to Assess the Impact of Vehicle-to-Grid Strategies on Battery Lifetime. *Appl. Energy* **2016**, *172*, 398–407. [CrossRef]
8. Tudoroiu, R.-E.; Zaheeruddin, M.; Tudoroiu, N.; Radu, S.M.; Chammas, H. *Investigations of Different Approaches for Controlling the Speed of an Electric Motor with Nonlinear Dynamics Powered by a Li-Ion Battery-Case Study*; IntechOpen: London, UK, 2023.
9. Tudoroiu, N.; Zaheeruddin, M.; Tudoroiu, R.-E.; Radu, M.S.; Chammas, H. Investigations on Using Intelligent Learning Techniques for Anomaly Detection and Diagnosis in Sensors Signals in Li-Ion Battery—Case Study. *Inventions* **2023**, *8*, 74. [CrossRef]
10. Mayyas, A.; Steward, D.; Mann, M. The Case for Recycling: Overview and Challenges in the Material Supply Chain for Automotive Li-Ion Batteries. *Sustain. Mater. Technol.* **2019**, *19*, e00087. [CrossRef]
11. Kale, R.B.; More, S.S.; Khupse, N.D.; Kalubarme, R.S.; Kulkarni, M.V.; Rane, S.B.; Kale, B.B. High-Voltage Ionic Liquid-Based Flexible Solid Polymer Electrolyte for High-Performance Li-Ion Batteries. *Sustain. Energy Fuels* **2023**, *7*, 2934–2942. [CrossRef]
12. Mai, L.; Li, L.; Yang, J.; Tan, R.; Shu, W.; Low, C.J.; Zhang, Z.; Zhao, Y.; Li, C.; Zhang, Y. Industrial-Scale Nonmetal Current Collectors Designed to Regulate Heat Transfer and Enhance Battery Safety. 2023. Available online: https://assets-eu.researchsquare.com/files/rs-3605453/v1_covered_a5fef811-9f7e-48f6-9ced-c6c8b8e0868a.pdf (accessed on 22 November 2024).
13. Ghosh, S.K.; Grover, A.K.; Dey, G.K.; Totlani, M.K. Nanocrystalline Ni–Cu Alloy Plating by Pulse Electrolysis. *Surf. Coat. Technol.* **2000**, *126*, 48–63. [CrossRef]

14. Sutopo, W.; Astuti, R.W.; Purwanto, A.; Nizam, M. Commercialization Model of New Technology Lithium Ion Battery: A Case Study for Smart Electrical Vehicle. In Proceedings of the 2013 Joint International Conference on Rural Information & Communication Technology and Electric-Vehicle Technology (rICT & ICeV-T), Bandung, Indonesia, 26–28 November 2013; IEEE: Piscataway, NJ, USA, 2013; pp. 1–5.
15. Hariharan, S.; Saravanan, K.; Ramar, V.; Balaya, P. A Rationally Designed Dual Role Anode Material for Lithium-Ion and Sodium-Ion Batteries: Case Study of Eco-Friendly Fe₃O₄. *Phys. Chem. Chem. Phys.* **2013**, *15*, 2945–2953. [[CrossRef](#)] [[PubMed](#)]
16. Speidel, M.O. Nitrogen Containing Austenitic Stainless Steels. *Mater. Und Werkst. Entwickl. Fert. Prüfung Eig. Und Anwendungen Tech. Werkst.* **2006**, *37*, 875–880. [[CrossRef](#)]
17. Ha, H.-Y.; Lee, T.-H.; Bae, J.-H.; Chun, D.W. Molybdenum Effects on Pitting Corrosion Resistance of FeCrMnMoNC Austenitic Stainless Steels. *Metals* **2018**, *8*, 653. [[CrossRef](#)]
18. Fande, A.W.; Taiwade, R.V. Welding of Super Duplex Stainless Steel and Austenitic Stainless Steel: Influence and Role of Bicomponent Fluxes. *Mater. Manuf. Process.* **2023**, *38*, 434–448.
19. Nilsson, J.-O. Super Duplex Stainless Steels. *Mater. Sci. Technol.* **1992**, *8*, 685–700. [[CrossRef](#)]
20. Michalska, J.; Chmiela, B. Phase Analysis in Duplex Stainless Steel: Comparison of EBSD and Quantitative Metallography Methods. In Proceedings of the IOP Conference Series: Materials Science and Engineering, Jakarta, Indonesia, 29–31 March 2014; IOP Publishing: Bristol, UK, 2014; Volume 55, p. 012010.
21. Valiente Bermejo, M.A.; Thalavai Pandian, K.; Axelsson, B.; Harati, E.; Kisielawicz, A.; Karlsson, L. Microstructure of Laser Metal Deposited Duplex Stainless Steel: Influence of Shielding Gas and Heat Treatment. *Weld. World* **2021**, *65*, 525–541. [[CrossRef](#)]
22. Nilsson, J.O.; Wilson, A. Influence of Isothermal Phase Transformations on Toughness and Pitting Corrosion of Super Duplex Stainless Steel SAF 2507. *Mater. Sci. Technol.* **1993**, *9*, 545–554. [[CrossRef](#)]
23. Kim, D.; Kim, S.; Park, J.; Kim, D.-I.; Shin, B.-H.; Yoon, J.-H. Effects of Passivation with Cu and W on the Corrosion Properties of Super Duplex Stainless Steel PRE 42. *Metals* **2024**, *14*, 284. [[CrossRef](#)]
24. Shin, B.-H.; Park, J.; Jeon, J.; Heo, S.; Chung, W. Effect of Cooling Rate after Heat Treatment on Pitting Corrosion of Super Duplex Stainless Steel UNS S 32750. *Anti-Corros. Methods Mater.* **2018**, *65*, 492–498. [[CrossRef](#)]
25. Köse, C.; Topal, C. Dissimilar Laser Beam Welding of AISI 2507 Super Duplex Stainless to AISI 317L Austenitic Stainless Steel. *Mater. Sci. Eng. A* **2023**, *862*, 144476. [[CrossRef](#)]
26. Saeid, T.; Abdollah-Zadeh, A.; Shibayanagi, T.; Ikeuchi, K.; Assadi, H. EBSD Investigation of Friction Stir Welded Duplex Stainless Steel. *World Acad. Sci. Eng. Technol.* **2010**, *61*, 376–379.
27. Mirzadeh, H.; Cabrera, J.M.; Najafzadeh, A.; Calvillo, P.R. EBSD Study of a Hot Deformed Austenitic Stainless Steel. *Mater. Sci. Eng. A* **2012**, *538*, 236–245. [[CrossRef](#)]
28. Fréchar, S.; Martin, F.; Clément, C.; Cousty, J. AFM and EBSD Combined Studies of Plastic Deformation in a Duplex Stainless Steel. *Mater. Sci. Eng. A* **2006**, *418*, 312–319. [[CrossRef](#)]
29. Barbosa, C.A.; Sokolowski, A. Development of UNS S 32760 Super-Duplex Stainless Steel Produced in Large Diameter Rolled Bars. *Rem Rev. Esc. De Minas* **2013**, *66*, 201–208. [[CrossRef](#)]
30. Paulraj, P.; Garg, R. Effect of Intermetallic Phases on Corrosion Behavior and Mechanical Properties of Duplex Stainless Steel and Super-Duplex Stainless Steel. *Adv. Sci. Technol. Res. J.* **2015**, *9*, 87–105. [[CrossRef](#)]
31. Soria, L.; Herrera, E.J. A Reliable Technique to Determine Pitting Potentials of Austenitic Stainless Steels by Potentiodynamic Methods. *Weld. Int.* **1992**, *6*, 959–964. [[CrossRef](#)]
32. Vignal, V.; Delrue, O.; Heintz, O.; Peultier, J. Influence of the Passive Film Properties and Residual Stresses on the Micro-Electrochemical Behavior of Duplex Stainless Steels. *Electrochim. Acta* **2010**, *55*, 7118–7125. [[CrossRef](#)]
33. Faraji, H.; Yıldız, Ç.; Arshad, A.; Arıcı, M.; Choukairy, K.; El Alami, M. Passive Thermal Management Strategy for Cooling Multiple Portable Electronic Components: Hybrid Nanoparticles Enhanced Phase Change Materials as an Innovative Solution. *J. Energy Storage* **2023**, *70*, 108087. [[CrossRef](#)]
34. Oh, S.; Kim, D.; Kim, K.; Kim, D.-I.; Chung, W.; Shin, B.-H. The Effect of Surface Roughness on Re-Passivation and Pitting Corrosion of Super Duplex Stainless Steel UNS S 32760. *Int. J. Electrochem. Sci.* **2023**, *18*, 100351. [[CrossRef](#)]
35. Saravanan, P.; Govindaraj, Y.; Khalkho, B.; Srikanth, S.; Kumar, V.; Neelakantan, L. Mechanical Properties and Corrosion Behaviour of Developed High Nitrogen High Manganese Stainless Steels. *Materwiss Werksttech* **2023**, *54*, 615–626. [[CrossRef](#)]
36. Metikoš-Huković, M.; Babić, R.; Grubač, Z.; Petrović, Ž.; Lajči, N. High Corrosion Resistance of Austenitic Stainless Steel Alloyed with Nitrogen in an Acid Solution. *Corros. Sci.* **2011**, *53*, 2176–2183. [[CrossRef](#)]
37. Jiang, S.; Xu, J.; Chen, Z.; Guo, R.; Miao, D.; Peng, L.; Wang, Y.; Shang, S. Enhanced Electro-Conductivity and Multi-Shielding Performance with Copper, Stainless Steel and Titanium Coating onto PVA Impregnated Cotton Fabric. *J. Mater. Sci. Mater. Electron.* **2018**, *29*, 5624–5633. [[CrossRef](#)]
38. Bogdan, D.; Grosu, I.-G.; Filip, C. How Thick, Uniform and Smooth Are the Polydopamine Coating Layers Obtained under Different Oxidation Conditions? An in-Depth AFM Study. *Appl. Surf. Sci.* **2022**, *597*, 153680. [[CrossRef](#)]

39. Rajesh, D.; Sunandana, C.S. XRD, Optical and AFM Studies on Pristine and Partially Iodized Ag Thin Film. *Results Phys.* **2012**, *2*, 22–25. [[CrossRef](#)]
40. Sen, S.K.; Paul, T.C.; Dutta, S.; Hossain, M.N.; Mia, M.N.H. XRD Peak Profile and Optical Properties Analysis of Ag-Doped h-MoO₃ Nanorods Synthesized via Hydrothermal Method. *J. Mater. Sci. Mater. Electron.* **2020**, *31*, 1768–1786. [[CrossRef](#)]
41. Standard, A. *Standard Test Method for Conducting Cyclic Potentiodynamic Polarization Measurements to Determine the Corrosion Susceptibility of Small Implant Devices*; ASTM International: West Conshohocken, PA, USA, 2019.
42. Isaacs, H.S.; Ishikawa, Y. Current and Potential Transients during Localized Corrosion of Stainless Steel. *J. Electrochem. Soc.* **1985**, *132*, 1288. [[CrossRef](#)]
43. Rehman, A.U.; Lee, S.H. Review of the Potential of the Ni/Cu Plating Technique for Crystalline Silicon Solar Cells. *Materials* **2014**, *7*, 1318–1341. [[CrossRef](#)]
44. Shin, B.-H.; Kim, D.; Park, S.; Hwang, M.; Park, J.; Chung, W. Precipitation Condition and Effect of Volume Fraction on Corrosion Properties of Secondary Phase on Casted Super-Duplex Stainless Steel UNS S32750. *Anti-Corros. Methods Mater.* **2018**, *66*, 61–66. [[CrossRef](#)]
45. Gasana, E.; Westbroek, P.; Hakuzimana, J.; De Clerck, K.; Priniotakis, G.; Kiekens, P.; Tseles, D. Electroconductive Textile Structures through Electroless Deposition of Polypyrrole and Copper at Polyaramide Surfaces. *Surf. Coat. Technol.* **2006**, *201*, 3547–3551. [[CrossRef](#)]
46. Guerrini, E.; Cristiani, P.; Grattieri, M.; Santoro, C.; Li, B.; Trasatti, S. Electrochemical Behavior of Stainless Steel Anodes in Membraneless Microbial Fuel Cells. *J. Electrochem. Soc.* **2013**, *161*, H62. [[CrossRef](#)]
47. Makhdoom, M.A.; Ahmad, A.; Kamran, M.; Abid, K.; Haider, W. Microstructural and Electrochemical Behavior of 2205 Duplex Stainless Steel Weldments. *Surf. Interfaces* **2017**, *9*, 189–195. [[CrossRef](#)]
48. Jo, H.; Ok, J.-W.; Lee, Y.-S.; Je, Y.; Kim, S.; Kim, S.; Park, J.; Lee, J.; Shin, B.-H.; Yoon, J.-H. Ag-Coated Super Duplex Stainless Steel AISI2507 with or without Crystallization of Secondary Phase as Advanced Li-Ion Battery Case Material. *Crystals* **2024**, *14*, 653. [[CrossRef](#)]
49. Amatsuka, S.; Nishimoto, M.; Muto, I.; Kawamori, M.; Takara, Y.; Sugawara, Y. Micro-Electrochemical Insights into Pit Initiation Site on Aged UNS S32750 Super Duplex Stainless Steel. *Npj Mater. Degrad.* **2023**, *7*, 15. [[CrossRef](#)]
50. Large, D.; Scandella, F.; Robineau, A.; Dupouiron, F.; Peultier, J.; Fanica, A.; Petit, B.; Thulin, A.; Pettersson, R.; Weisang-Hoinard, F. Welding of Lean Duplex Stainless Steel Grades: Microstructure, Corrosion Resistance and Mechanical Properties. In Proceedings of the NACE CORROSION (NACE 2012), Salt Lake City, UT, USA, 11–15 March 2012; p. NACE-2012.
51. Vongsilathai, S.; Lothongkum, A.W.; Lothongkum, G. Corrosion Behavior of a New 25Cr-3Ni-7Mn-0.66 N Duplex Stainless Steel in Artificial Seawater. *Materials Testing* **2021**, *63*, 505–511.
52. Rybalka, K.V.; Beketaeva, L.A.; Davydov, A.D. Electrochemical Behavior of Stainless Steel in Aerated NaCl Solutions by Electrochemical Impedance and Rotating Disk Electrode Methods. *Russ. J. Electrochem.* **2006**, *42*, 370–374. [[CrossRef](#)]
53. Lim, J.; Shin, B.-H.; Kim, D.-I.; Bae, J.-S.; Ok, J.-W.; Kim, S.; Park, J.; Lee, J.I.; Yoon, J.-H. Effect of Annealing after Casting and Cold Rolling on Microstructure and Electrochemical Behavior of High-Entropy Alloy, Cantor. *Metals* **2024**, *14*, 846. [[CrossRef](#)]

Disclaimer/Publisher’s Note: The statements, opinions and data contained in all publications are solely those of the individual author(s) and contributor(s) and not of MDPI and/or the editor(s). MDPI and/or the editor(s) disclaim responsibility for any injury to people or property resulting from any ideas, methods, instructions or products referred to in the content.